Saturated Double-Angle Method for Rapid B_1+ Mapping

Charles H. Cunningham,[1] John M. Pauly,[1] and Krishna S. Nayak[2]*

For in vivo magnetic resonance imaging at high field (≥3 T) it is essential to consider the homogeneity of the active B_1 field (B_1+), particularly if surface coils are used for RF transmission. A new method is presented for highly rapid B_1+ magnitude mapping. It combines the double angle method with a B_1-insensitive magnetization-reset sequence such that the choice of repetition time (TR) is independent of T_1 and with a multislice segmented (spiral) acquisition to achieve volumetric coverage with adequate spatial resolution in a few seconds. Phantom experiments confirmed the accuracy of this technique even when TR $\ll T_1$, with the side effect being lowered SNR. The speed of this method enabled B_1+ mapping in the chest and abdomen within a single breath-hold. In human cardiac imaging, the method enabled whole-heart coverage within a single 16-s breath-hold. Results from phantoms and healthy volunteers at 1.5 T and 3 T are presented. Magn Reson Med 55:1326–1333, 2006. © 2006 Wiley-Liss, Inc.

Key words: B_1+ mapping; double-angle method; high-field imaging; body MRI; spirals

For in vivo MRI at high field (≥3 T) it is essential to consider the homogeneity of the active B_1 field (B_1+), particularly if surface coils are used for RF transmission. The B_1+ field is the transverse, circularly polarized component of B_1 that is rotating in the same sense as the magnetization. When exciting or manipulating large collections of spins, nonuniformity in B_1+ results in nonuniform treatment of spins. This leads to spatially varying image signal and image contrast and to difficulty in image interpretation and image-based quantification. The B_1+ field experienced by spins within the body is influenced by several factors including the distance from the RF transmit coil, tissue dielectric constant, and factors related to the body size and RF wavelength. In high-field (≥3 T) abdominal, cardiac, and neuro imaging, B_1+ inhomogeneity on the order of 30–50% has been predicted and observed (1–4). When using surface coil transmission, even greater variations in B_1+ can be observed over typical imaging FOVs (5,6).

There are several existing B_1+ mapping methods based on measurements at progressively increasing flip angles (7), stimulated echoes (8), or signal ratios (5,9–14). The most simple and straightforward of these methods is the double-angle method, which involves acquiring images with two flip angles α and 2α, where TR $\gg T_1$ such that image signal is proportional to sin(α) and sin(2α), respectively. The B_1+ field is derived from the ratio of signal magnitudes. Previous double-angle approaches (9,10,12) have been limited by the requirement of long TRs and therefore long imaging times and motion compensation issues. While accurate in static body regions, these methods are not practical in areas of the body that experience motion, such as the chest and abdomen.

The proposed method combines a double-angle method with (1) a B_1-insensitive magnetization reset sequence at the end of each data acquisition, which lifts the dependence of TR on T_1 and enables rapid imaging, and (2) an interleaved spiral readout (15,16), enabling multislice acquisition of B_1+ maps in a short time (a single breath-hold). Phantom and in vivo validation data are presented along with B_1+ homogeneity measurements in the heart at 3 T.

THEORY

The proposed method uses an adaptation of the double angle method (DAM) described previously (9,10). Such methods allow calculation of a flip-angle map, which is an indirect measure of the B_1+ field. Two images are acquired: I_1 with prescribed tip angle α_1 and I_2 with prescribed tip angle $\alpha_2 = 2\alpha_1$. All other signal-affecting sequence parameters are kept constant. For each voxel, the ratio of magnitude images satisfies

$$\frac{I_2(r)}{I_1(r)} = \frac{\sin\,\alpha_2(r)\, f_2(T_1, \mathrm{TR})}{\sin\,\alpha_1(r)\, f_1(T_1, \mathrm{TR})},$$

where r represents spatial position and $\alpha_1(r)$ and $\alpha_2(r)$ are tip angles that vary with the spatially varying B_1+ field. If the effects of T_1 and T_2 relaxation can be neglected, then the actual tip angles as a function of spatial position satisfy

$$\alpha(r) = \arccos\left(\left|\frac{I_2(r)|}{2I_1(r)}\right|\right).$$

A long repetition time (TR ≥5 T_1) is typically used with the double-angle methods so that there is no T_1 dependence in either I_1 or I_2 (i.e., $f_1(T_1,\mathrm{TR}) = f_2(T_1,\mathrm{TR}) = 1.0$). Instead, the proposed method includes a magnetization-reset sequence after each data acquisition with the goal of putting the spin population in the same state regardless of whether the α or 2α excitation was used for the preceding acquisition (i.e., $f_1(T_1,\mathrm{TR}) = f_2(T_1,\mathrm{TR}) \neq 1.0$).

The RF pulse used for saturation of the magnetization must destroy M_z over a range of B_1+ values since this sequence is intended for use in areas with inhomogeneous B_1+. Two classes of RF pulses that meet this requirement were investigated: composite pulse trains (17) and BIR4

[1]Magnetic Resonance Systems Research Laboratory, Department of Electrical Engineering, Stanford University, Stanford, California.

[2]Magnetic Resonance Engineering Laboratory,Department of Electrical Engineering–Systems, University of Southern California, Los Angeles, California.

Grant sponsor: American Heart Association; Grant number: 0435249N; Grant sponsor: National Institutes of Health; Grant number: R01-HL074332; Grant sponsor: James H. Zumberge Foundation; Grant sponsor: GE Healthcare.

*Correspondence to: Krishna S. Nayak, Electrical Engineering–Systems, 3740 McClintock Avenue, EEB 406, University of Southern California, Los Angeles, CA 90089-2564. E-mail: knayak@usc.edu

Received 6 July 2005; revised 12 December 2005; accepted 13 February 2006

DOI 10.1002/mrm.20896

Published online 8 May 2006 in Wiley InterScience (www.interscience.wiley.com).

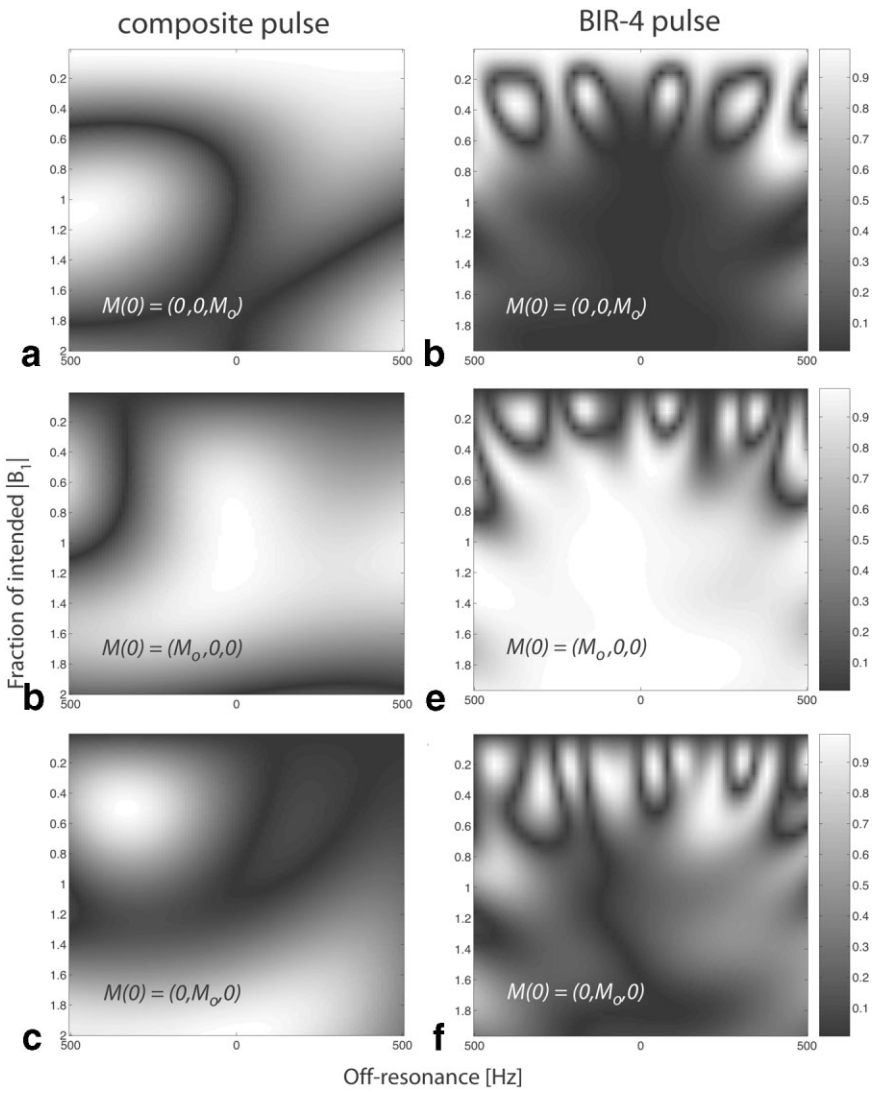

FIG. 1. Bloch equation simulations showing the performance of B_1-insensitive saturation pulses: (**a–c**) The residual longitudinal magnetization after application of a 1.2-ms 45_x–90_y–90_x–(-45_y) composite pulse. The direction of the magnetization before each pulse is shown on the plots. (**d–f**) The residual longitudinal magnetization after application of an 8-ms BIR-4 pulse (hyperbolic secant envelope with $\lambda = 5$, $\beta = 1.6$ as defined in (18)). Both pulses saturate M_z and leave M_y in the transverse plane (dark regions) as desired, but tip M_x back to the longitudinal axis (see b and e). The consequence of this is discussed in Theory.

pulses (18). The performance of these waveforms as saturation pulses is shown in Fig. 1. The particular BIR4 pulse investigated is much better in terms of insensitivity to B_1+ and B_0 inhomogeneity, but comes at the price of a sixfold increase in the pulse duration and in the anticipated specific absorption rate (SAR). An undesired feature of both pulses is that both tip some magnetization back onto the longitudinal axis (see Fig. 1b and e). To reduce the resulting T_1 weighting, T_2 decay can be relied upon to eliminate this component, or the saturation pulse can be applied multiple times, with crushers in between each pulse.

METHODS

Imaging Sequence

The pulse sequence (illustrated in Fig. 2) consists of an imaging sequence and a magnetization reset sequence. The imaging sequence contains a tip pulse, readout, and gradient spoiler, while the reset sequence contains a nonselective saturation pulse (17) (which is insensitive to both B_1 variations and off-resonance) and a gradient spoiler. The prescribed flip angles prescribed are $\alpha_1 = 60°$ and $\alpha_2 = 120°$. In our experiments, spiral readouts were chosen because of their efficiency, good flow properties, and short echo time; however, alternate *k*-space segmentations such as echo planar imaging (EPI) (19) may be substituted. The spiral readouts were 16 ms in duration, and only a portion of those data were used during reconstruction depending on off-resonance, resolution, and SNR considerations. Gridding reconstruction (non-Cartesian sampling) and coil combination (multicoil imaging) was performed prior to "double-angle" processing.

Because B_1+ profiles are usually quite smooth, in cases where SNR was lacking, we opted to use only the first 4 or 8 ms of each readout, which maintains the same FOV, but reduces the spatial resolution ($\Delta x\, \Delta y$) and reduces the total readout time T_{read}. The net effect on SNR is an increase. To reduce ringing artifacts caused by *k*-space truncation, a radial Hamming window was applied to gridded *k*-space data before inverse Fourier-transforming.

As shown in Fig. 2, the acquisitions contributing to I_1 and I_2 are interleaved and can be cardiac gated if necessary. Multiple slices are covered sequentially in each repetition and can share a single contrast preparation pulse

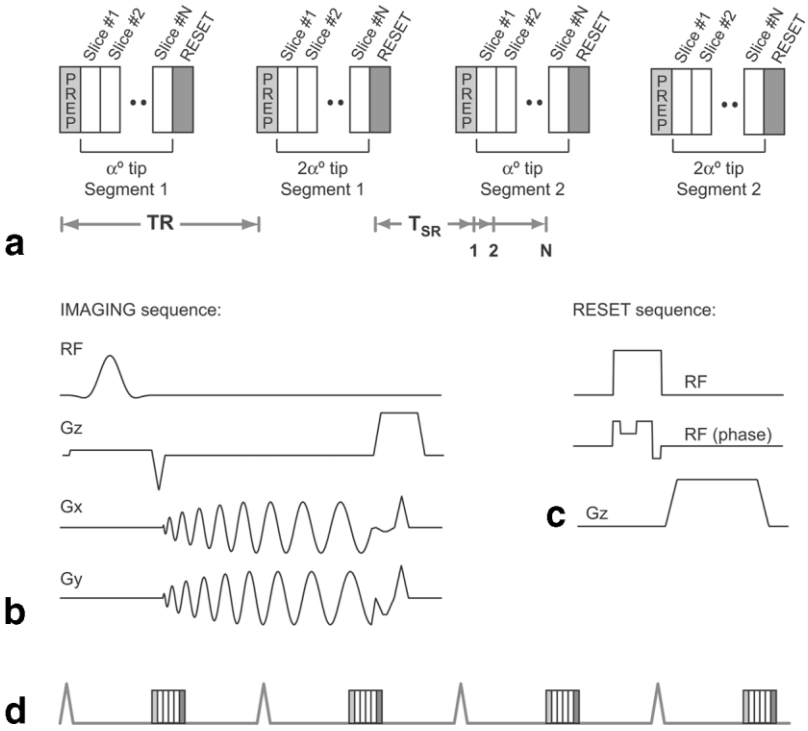

FIG. 2. SDAM pulse sequence with spiral acquisitions. Full images are acquired with a prescribed α and prescribed 2α flip angle. A B_1-insensitive saturation pulse is used to reset the magnetization after each acquisition set. The acquisition of multiple slices is achieved as shown in (**a**). Contrast preparation such as a FAT-SAT can be used prior to imaging. The (**b**) imaging sequence consists of a simple slice-selective excitation, followed by a short spiral readout, and a dephaser. The (**c**) reset sequence consists of a B_1-insensitive and nonspatially selective saturation pulse followed by a dephaser. As shown in (**d**) acquisitions can also be cardiac gated, to prevent cardiac motion artifacts.

(such as a FATSAT) and share a single nonselective magnetization saturation pulse as shown. The imaging excitations are slice selective, while the contrast preparation and saturation pulses are not spatially selective.

Experimental Methods

Studies were performed on GE Signa 1.5T and 3T scanners (GE Healthcare, Waukesha, WI, USA) with EXCITE hardware. Both scanners were equipped with gradients capable of 40 mT/m amplitude and 150 T/m/s slew rate and a receiver capable of 2-μs sampling ($\pm$250 kHz). The composite saturation pulse tested in Fig. 1 was used in all SDAM measurements. In phantom studies, a head coil was used for RF transmission and reception. In static in vivo validation studies either a head coil or extremity coil was used for RF transmission and reception. In abdominal and cardiac studies, a body coil was used for RF transmission and four-channel phased array coil was used for signal reception. Synchronization with the cardiac cycle was achieved with prospective triggering based on an infrared plethysmograph that monitors blood volume in a finger (20). The institutional review boards of Stanford University and the University of Southern California approved the imaging protocols. Each subject was screened for mag-

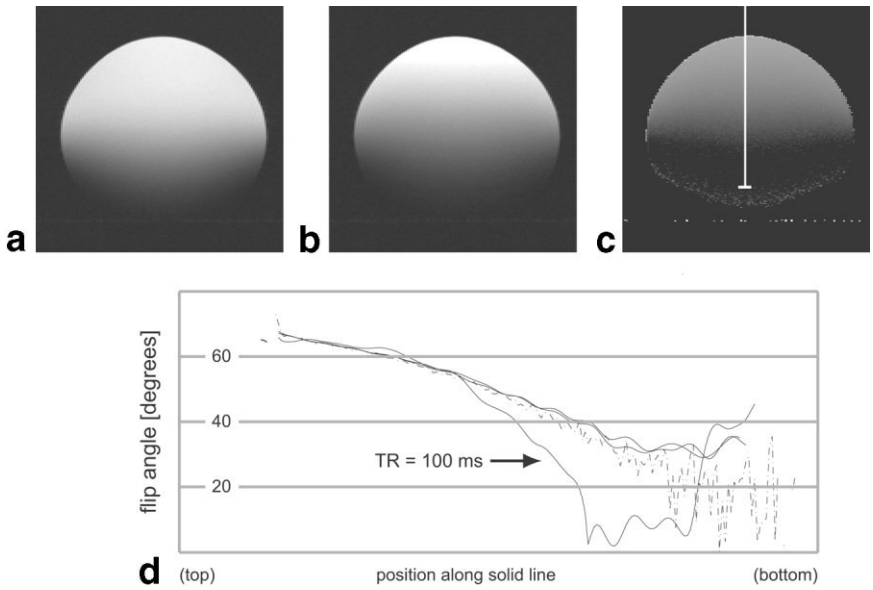

FIG. 3. Phantom validation study: A large ball phantom (T_1 of 345 ms) was centered at the end of the birdcage head coil. Half of the phantom was within the coil, and half was outside. The top row contains (**a**) the 2α flip angle image, (**b**) the α flip angle image, and (**c**) the computed flip angle map, all with TR = 3 s and with a line showing the column plotted in (**d**). Plots of the flip angle variation are shown in (d), with the dashed line showing the reference (long TR) and the solid lines showing measurements with SDAM with TR of 1000, 500, and 100 ms overlapping. The discrepancy between the 100-ms curve and the others is discussed in the text. The scan time with 500 ms TR was 8 s. The in-plane resolution was 2 mm and the slice thickness was 5 mm.

netic resonance imaging risk factors and provided informed consent in accordance with institutional policy.

To validate the accuracy of the method, B_1+ measurements were made in a phantom and normal volunteers. In the phantom study, the new method was used with TR ranging from 1 s to 100 ms. This was compared with a reference double-angle method consisting of two sequential gradient-echo scans using a long TR of 3 s and Cartesian *k*-space sampling. The phantom was spherical with 18 cm diameter and consisted of distilled water doped with copper sulfate. The T_1 of the phantom was 345 ms as measured using an inversion-recovery sequence. A quadrature transmit/receive head coil was used, with the phantom positioned halfway out the end of the coil to produce an inhomogeneous B_1+. A linear transmit/receive extremity coil was used to produced a B_1+ map in the leg of a normal volunteer, both with the new method and the reference double-angle method with a long TR (3 s). The B_1+ field was inhomogeneous where the leg extended beyond the coil. Last, for comparison with previous studies (4), measurements were made of the B_1+ homogeneity in a human head at 3 T using a standard birdcage head coil for RF transmission and signal reception. Maps made with TRs ranging from 3000 to 400 ms were compared.

Abdominal B_1+ maps covering the lower liver were acquired in two healthy volunteers at 3 T. Scan planes were localized using a standard three-plane localizer, and six axial slices were prescribed spanning the liver. Fat saturation was used in both subjects. B_1+ maps of six slices were acquired in a 16-s scan with a 1-s TR (8 spiral interleaves × 2 flip angles). This was repeated with a 500-ms TR (8-s scan) and 250-ms TR (4-s scan).

Cardiac B_1+ maps were acquired in four healthy volunteers at 3 T. Short-axis and long-axis views were localized using the GE I-drive real-time system. In each volunteer, eight parallel short axis slices were prescribed spanning the left ventricle from base to apex (base was slice 1 and apex was slice 8). Fat saturation was used in all subjects. Acquisitions were cardiac gated (using a plethysmograph), with imaging occurring in mid-diastole, and were performed during breath-holds. Whole-heart coverage was achieved in a single breath-hold of 20 R-R intervals (14 to 25 s with heart rates of 48 to 85 beats/min).

RESULTS

Static Validation

Figure 3 contains images and flip angle profiles from the ball phantom experiment with the ball at the edge of a transmit-receive head coil, producing a highly inhomogeneous B_1+ field. The flip angle profiles measured with the reference method and with SDAM are shown in Fig. 3d. Good agreement with the reference method (dashed line) was observed. As TR is reduced, the SNR decreases (due to reduced T_1 recovery time), but there is no identifiable distortion in the flip angle profile. The curve for TR = 100 ms deviates from the others in the region with very low SNR. This was investigated and was found to result from low-amplitude artifacts in the spiral images. These artifacts are likely due to system instabilities and only became significant relative to the desired signal when the SNR is low.

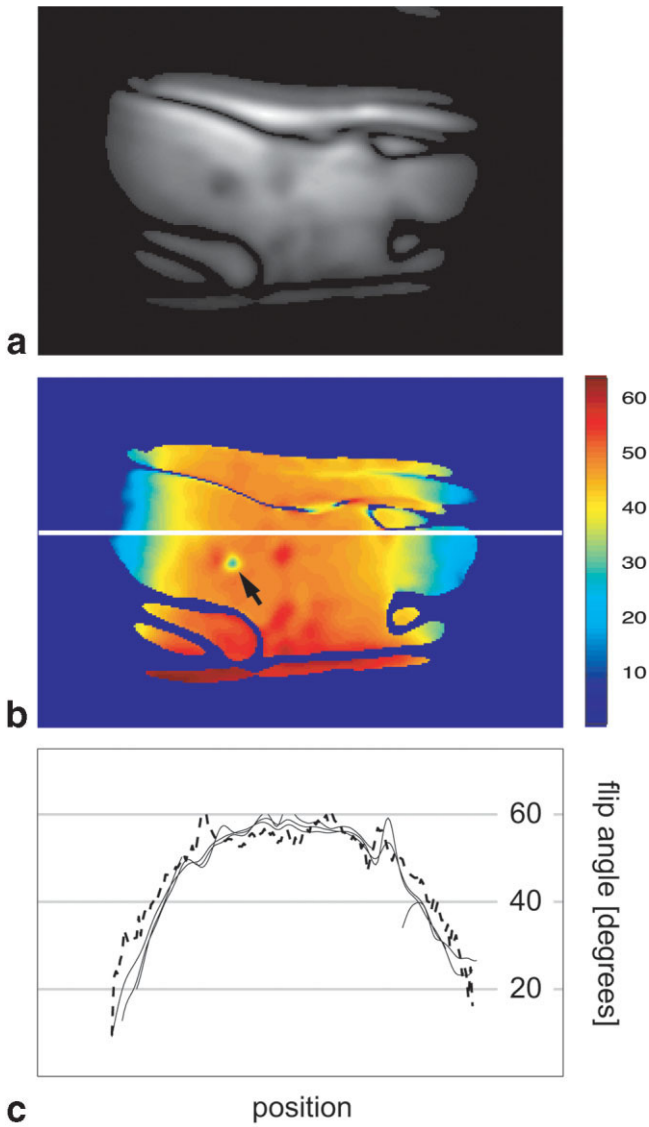

FIG. 4. Validation in a human leg at 1.5 T: (**a**) anatomic image, (**b**) B_1+ map, (**c**) B_1+ profiles along the line shown in (b) using DAM (TR = 3 s, dashed line), and SDAM with TR = 1 s, 500 ms, and 100 ms (solid lines). The arrow indicates a region with short T_2 where an error in the B_1 map occurs. The scan time with TR of 100 ms was 1.6 s. The in-plane spatial resolution after windowing was 7 mm and the slice thickness was 5 mm.

Figure 4 contains images and flip angle profiles from the human leg experiment in the extremity coil. Again, the profiles collected with SDAM (Fig. 4c) show excellent agreement with each other and with the reference. As TR is reduced, the SNR moderately decreases, as expected. It is interesting to note that tissues with sufficiently short T_2 cause an error in the B_1+ map (arrow) because, for these tissues, flip angle will not scale linearly with RF amplitude (21).

Figure 5 contains images and flip angle profiles from a human head scan at 3 T. The SDAM profiles collected with TR of 2 s and 400 ms show excellent agreement, even for TR < T_1. The anatomic image shows the expected center brightening that can result from dielectric effects (22), and

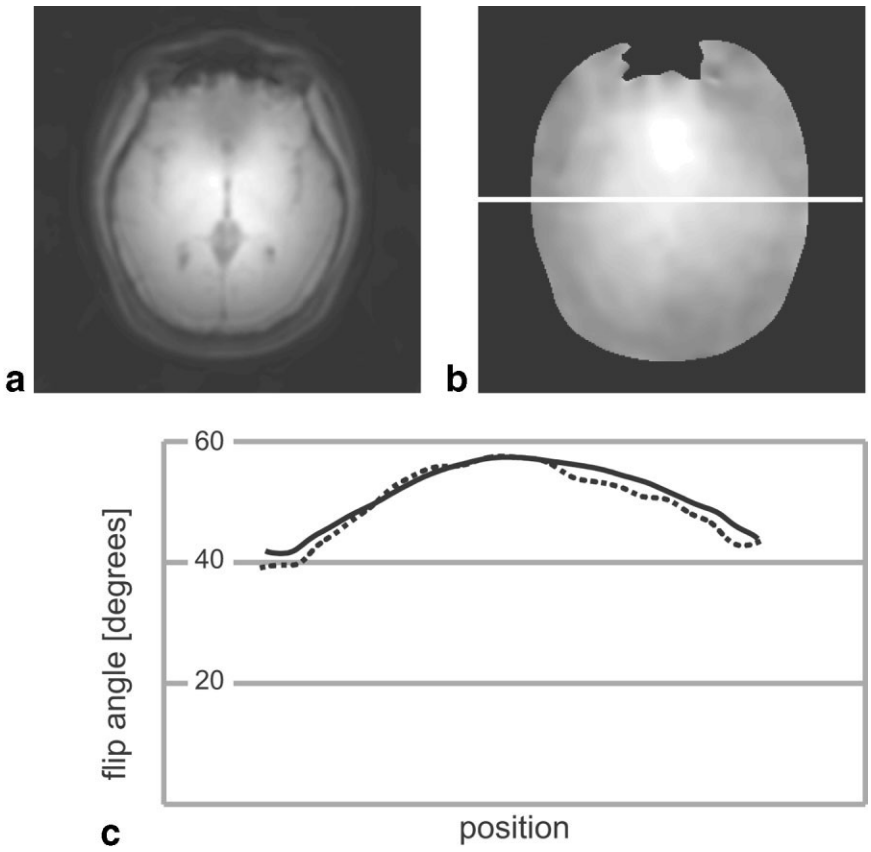

FIG. 5. Validation in a human head at 3 T. (**a**) The α image and (**b**) the computed flip angle map and (**c**) plots of the flip angle variation in the left/right direction, acquired with SDAM with TR of 2000 (solid) and 400 ms (dashed). The scan time with TR of 400 ms was 10 s. The images in (a,b) are from the TR = 2000 ms scan. As expected, the B_1+ profile is parabolic in shape. The in-plane spatial resolution after windowing was 4.2 mm and the slice thickness was 5 mm.

the flip angle map shows a corresponding elevation toward the center of the head. It should be noted that the center-brightening seen in Fig. 5a is due to a combination of the effects of B_1+ during transmit and B_1- during signal acquisition (23), with the spatial pattern for each being different. By using the ratio of signals, the B_1- distribution is factored out in double-angle methods such as SDAM. The observed flip angle elevation is in agreement with other published flip angle measurements in the head at 3 T (4).

Breath-Held Measurements

Representative abdominal B_1+ maps from one volunteer are shown in Fig. 6. Six slices were acquired in a single breath-hold. Focusing on the the fourth slice, Fig. 6 con-

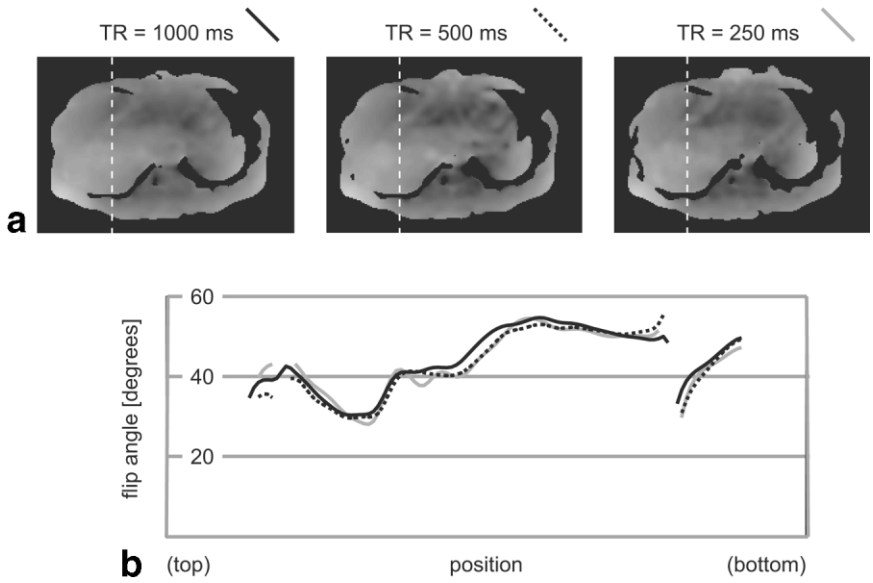

FIG. 6. Abdominal B_1+ maps in a healthy volunteer at 3 T with short repetition times. A six-slice acquisition was repeated with TR = 1 s, 500 ms, and 250 ms, with acquisition time of each scan being 16 $\times$ TR. Flip angle maps (black = 0°, white = 60°) of slice 4 from all three datasets are shown in (**a**), with the flip angles along the dotted line plotted in (**b**). Note that the flip angle maps retain accuracy even for short TRs, with the primary side effect being lowered SNR due to the shorter saturation recovery time. The in-plane spatial resolution after windowing was 10 mm and the slice thickness was 5 mm.

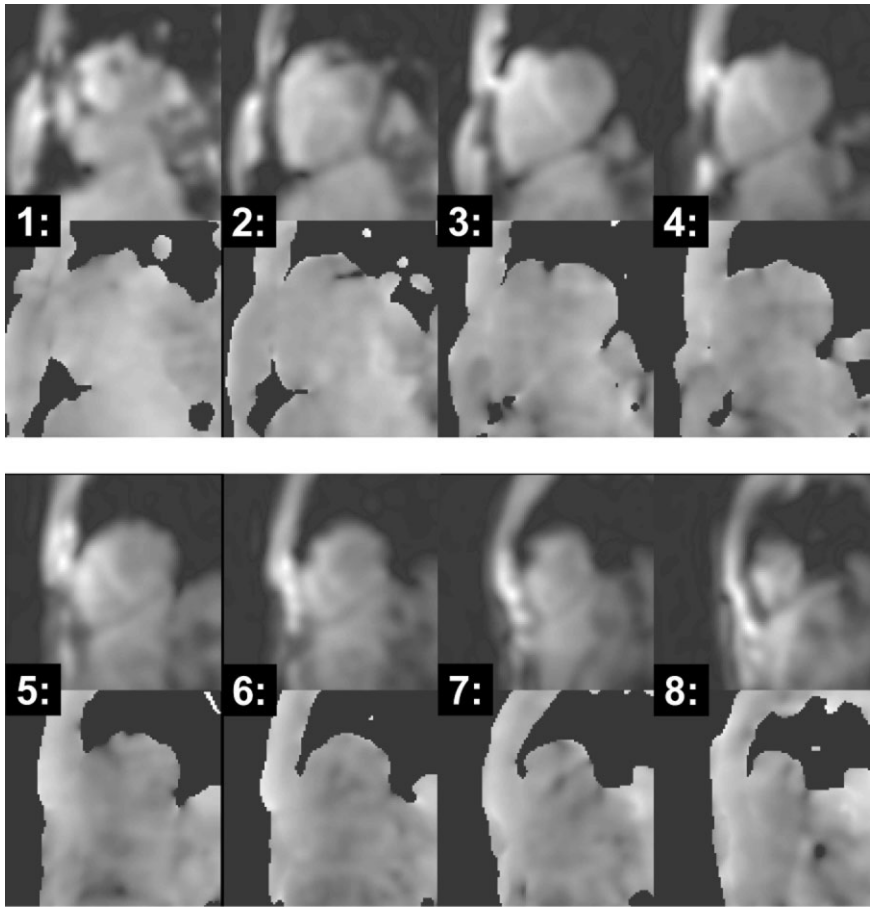

FIG. 7. Cardiac B_1+ maps in a healthy volunteer at 3 T. B_1+ maps of eight parallel slices were acquired in one 18-s breathhold. For each slice, magnitude images (top row) and flip angle maps (bottom row) are shown with black = 0° and white = 60°. Note that the eight slices are of slightly different cardiac phase and that SNR is sufficiently high. The in-plane resolution after windowing was 10 mm and the slice thickness was 5 mm.

tains the flip angle maps derived using the three different TRs. Except for moderately decreased SNR, there were no identifiable artifacts observed when TR was shortened.

Representative cardiac B_1+ maps are shown in Figs. 7 and 8. Magnitude images and flip angle maps for all slices are shown in Fig. 7. Focusing on a mid-short axis slice (slice 4), Fig. 8 contains magnitude images for I_1 and I_2, along with the derived flip angle map. Plotting a line through the image, B_1+ appears to decrease for locations further from the chest wall and rise again closer to the midpoint of the body. It is also interesting to note that for a prescribed flip angle of 60° (with transmit gain calibrated

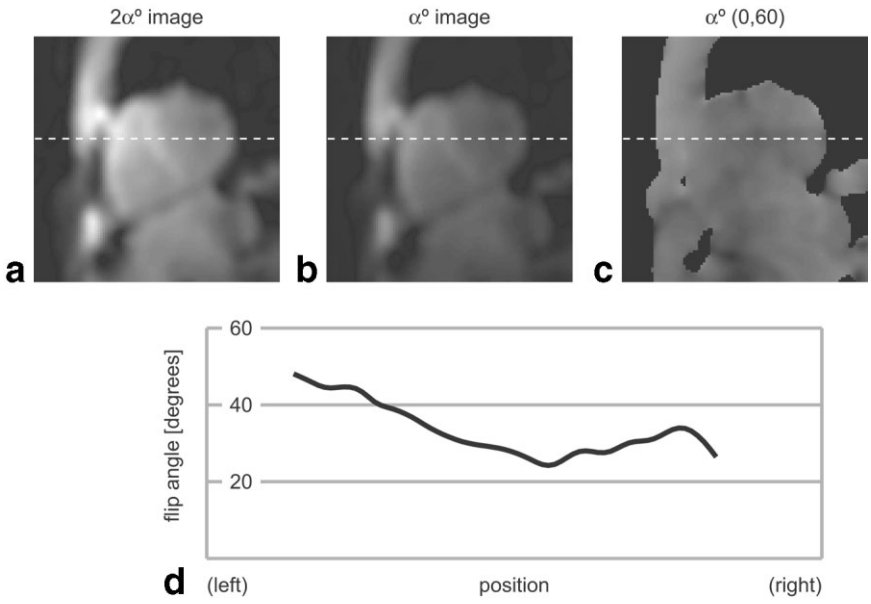

FIG. 8. Cardiac B_1+ maps in a healthy volunteer at 3 T. (**a–c**) show the magnitude images and flip angle map from a mid short axis slice (slice 4 from Fig. 7). The flip angles along the dotted line are shown in (d), illustrating experienced flip angles between 22 and 50°, when a 60° flip angle was prescribed. The in-plane resolution after windowing was 10 mm and the slice thickness was 5 mm.

using standard prescan), the flip angles experienced by myocardium were actually in the 25–45° range, which is a substantial deviation.

The level of inhomogeneity observed (100%) and the general shape of B_1+ variation are consistent with published references (3), and with SDAM, were acquired in substantially shorter scan time.

DISCUSSION

SNR of the acquired images is dependent on the saturation recovery time T_{SR}, with image SNR $\propto 1 - e^{-T_{SR}/T_1}$. As a natural consequence, shorter TRs result in lower T_{SR} (see Fig. 2a), lower SNR, and noisier B_1+ maps. In addition, because the different slices in a multislice acquisition have different recovery times, SNR of the B_1+ maps increases from the first slice to the last. When using a very short TR, it may be beneficial to place the most important slices last in the multislice acquisition block (see Fig. 2). In addition, the double-angle method uses a nonlinear computation, Eq. [2], which results in further noise amplification in areas where $\alpha(r)$ is small (near 0°) or large (near 90°). To mitigate problems associated with low SNR the image resolution was limited to pixel sizes of several millimeters. This was done by applying a Hamming window to the *k*-space data in order to truncate the data without causing a ringing artifact. Because of the circular *k*-space coverage, a Hamming window that varied with the radial distance was used. The effect of this windowing operation is a slightly lower spatial resolution than would be expected from the extent of the data in *k*-space (24). This effect will be negligible in most cases because B_1+ variations are typically smooth.

The key component of the proposed sequence is the robust magnetization saturation. The effectiveness of the saturation used in these experiments was demonstrated by varying the TR and this showed negligible change in the B_1+ maps. Although a short composite pulse was used here, there are many possibilities for saturation pulses that are insensitive to B_1 and B_0 inhomogeneity and the appropriate pulse can be chosen for different applications. It is likely that the most robust method would be a long train of adiabatic refocusing pulses; howeve, this would come at a price in minimum TR and RF heating. The basic idea of resetting the magnetization to remove T_1 weighting could be extended to other methods for measuring B_1+ as well, such as phase-based methods in which the flip angle is converted into phase in the transverse plane by applying a 90° (B_1+ insensitive) plane-rotation pulse (25).

With very short TR, such as when TR $\ll T_2$, there is a possibility that stimulated echoes could form. These can be avoided by modulating the size of the dephaser after the saturation pulse. Given that the total number of applications of the saturation pulse is not large (twice the number of spiral interleaves), dephasers with relative areas that are geometrically increased could be used to remove the possibility of stimulated echoes.

The current multislice acquisition may be affected by flow between acquisitions. The use of a spatially nonselective saturation pulse alleviates this problem to some degree, as all magnetization within the sensitive region of the transmit coil (and within the parameters of the particular saturation pulse; see Fig. 1) will be saturated. However, spins from adjacent slices may flow into one another during the multislice acquisition, disturbing the steady state established by the saturation pulse. However, this effect will be fairly consistent from measurement to measurement if cardiac gating is used. If flow is irregular, B_1+ estimates in blood or regions of flow may be discarded. This is not an issue for single-slice mapping.

For cardiac applications, there is the consideration of arrhythmia, or otherwise irregular R-R intervals. This will cause unequal amounts of saturation recovery time among *k*-space segments, which can result in image artifacts, and errors in the B_1+ maps that have not been yet been analyzed. Also, our initial implementation requires a breathhold, which some patients may not be able to perform. However, with the introduction of a navigated acquisition, these limitations can be alleviated.

There are numerous applications for B_1+ information that are anticipated to be useful. One possibility is adjusting the RF power dynamically to achieve the desired flip angle in regions of interest. Also, it is possible to design RF pulses "on-the-fly" to compensate for smoothly varying B_1+ components (4,26). For some applications, such as transmit SENSE (27,28), a flip-angle dynamic range may be required that is larger than that supported with the arccos relationship of Eq. [2] (about 20 dB). In this case, the method could be applied multiple times, with the flip angle increased upon successive measurements to improve the dynamic range. The speed of the method makes such multiple acquisition schemes feasible. Besides the flip angle, the phase of the B_1+ field may also be desired. To do this, an additional data acquisition could be performed using an adiabatic half-passage for the excitation pulse (25). The *x*- and *y*-components of the resulting magnetization would correspond to the *x*- and *y*-components of B_1+.

CONCLUSIONS

B_1+ mapping is becoming an integral part of prescan calibration in high-field MRI and MRI with surface transmit coils. The SDAM can yield volumetric B_1+ maps with adequate spatial resolution in just a few seconds. This has substantial implications for high-field neuroimaging and for the first time enables rapid cardiac and abdominal B_1+ mapping within the duration of a breath-hold (necessary for time-efficient motion suppression).

REFERENCES

1. Singerman RW, Denison TJ, Wen H, Balaban RS. Simulation of B_1 field distribution and intrinsic signal-to-noise in cardiac MRI as a function of static magnetic field. J Magn Reson 1997;125:72–83.
2. Wen H, Denison TJ, Singerman RW, Balaban RS. The intrinsic signal-to-noise ratio in human cardiac imaging at 1.5, 3, and 4 T. J Magn Reson 1997;125:65–71.
3. Greenman RL, Shirosky JE, Mulkern RV, Rofsky NM. Double inversion black-blood fast spin-echo imaging of the human heart: a comparison between 1.5T and 3.0T. J Magn Reson Imaging 2003;17:648–655.
4. Saekho S, Boada FE, Noll DC, Stenger VA. Small tip angle three-dimensional tailored radiofrequency slab-select pulse for reduced *B*1 inhomogeneity at 3 T. Magn Reson Med 2005;53:479–484.

5. Wang J, Qiu M, Yang QX, Smith MB, Constable RT. Measurement and correction of transmitter and receiver induced nonuniformities in vivo. Magn Reson Med 2005;53:408–417.
6. Deichmann R. Optimized rf excitation for anatomical brain imaging of the occipital lobe using the 3D MDEFT sequence and a surface transmit coil. Magn Reson Med 2005;53:1212–1216.
7. Hornak JP, Szumowski J. Magnetic field mapping. Magn Reson Med 1988;6:158–163.
8. Akoka S, Frankoni F, Seguin F, Pape AL. Radiofrequency map of an NMR coil by imaging. Magn Reson Imaging 1993;11:437–441.
9. Stollberger R, Wach P, McKinnon G, Justich E, Ebner F. Rf-field mapping in vivo. In: Proceedings of the 7th Annual Meeting of SMRM, San Francisco, CA, USA, 1988. p. 106.
10. Insko EK, Bolinger L. B_1 mapping. In: Proceedings of the 11th Annual Meeting of SMRM, Berlin, Germany, 1992. p. 4302.
11. Insko EK, Bolinger L. Mapping of the radiofrequency field. J Magn Reson A 1993;103:82–85.
12. Stollberger R, Wach P. Imaging of the active B_1 field in vivo. Magn Reson Med 1996;35:246–251.
13. Yarnykh VL, Yuan C. Actual flip angle imaging in the pulsed steady state. In: Proceedings of the 12th Annual Meeting of ISMRM, Kyoto, Japan, 2004. p. 194.
14. Maier JK, Glover GH. Method for mapping the rf transmit and receive field in an NMR system. U. S. Patent 5001428, 1991.
15. Ahn CB, Kim JH, Cho ZH. High-speed spiral-scan echo planar NMR imaging–I. IEEE Trans Med Imaging 1986; MI-5:2–7.
16. Meyer CH, Hu BS, Nishimura DG, Macovski A. Fast spiral coronary artery imaging. Magn Reson Med 1992;28:202–213.
17. Levitt MH. Composite pulses. Progr NMR Spectrosc 1986;18:61–122.
18. Staewen RS, Johnson AJ, Ross BD, Parrish T, Merkle H, Garwood M. 3-D FLASH imaging using a single surface coil and a new adiabatic pulse, BIR-4. Invest Radiol 1990;25:559–567.
19. Mansfield P. Multi-planar image formation using NMR spin echoes. J Phys C 1977;10:580–594.
20. Hokanson DE, Sumner DS, Strandness DE Jr. An electrically calibrated plethysmograph for direct measurement of limb blood flow. IEEE Trans Biomed Eng 1975;22:25–29.
21. Pauly JM, Conolly SM, Nishimura DG. Magnetic resonance imaging of short T_2 species with improved contrast. U. S. Patent 5150053:1992.
22. Hoult DI. Sensitivity and power deposition in a high-field imaging experiment. J Magn Reson Imaging 2000;12:46–67.
23. Collins CM, Yang QX, Wang JH, Zhang X, Liu H, Michaeli S, Zhu X, Adriany G, Vaughan JT, Anderson P, Merkle H, Ugurbil K, Smith MB, Chen W. Different excitation and reception distributions with a single-loop transmit-receive surface coil near a head-sized spherical phantom at 300 MHz. Magn Reson Med 2002;47:1026–1028.
24. Bracewell RN, The Fourier transform and its applications. New York: McGraw–Hill, 1986.
25. Scott GC, Joy MLG, Armstrong RL, Henkelman RM. Electromagnetic considerations for RF current density imaging. IEEE Trans. Med Imaging 1995;14:515–524.
26. Sung K, Nayak KS. *B*1+ non-uniformity correction using 2D RF pulse design. In: Proceedings of the 13th Annual Meeting of ISMRM, Miami Beach, FL, USA, 2005. p. 18.
27. Katscher U, Bornert P, Leussler C, van den Brink JS. Transmitt SENSE. Magn Reson Med 2003;49:144–150.
28. Zhu Y. Parallel excitation with an array of transmit coils. Magn Reson Med 2004;51:775–784.